


 Cite this: *Lab Chip*, 2026, 26, 3002

 Received 12th March 2026,  
 Accepted 14th April 2026

DOI: 10.1039/d6lc00230g

[rsc.li/loc](https://rsc.li/loc)

## Porous microneedle-based electrochemical aptamer biosensor for the collection and quantitative analysis of dry eye disease biomarkers

 Eira Beryle Ko,<sup>†</sup> Tianli Hu,<sup>†</sup> Ya Zhang, Xueyan Wang, Yu Song\* and Chenjie Xu \*

Dry eye disease (DED) is a prevalent ocular disorder driven by tear film instability and inflammation. The quantitative measurement of molecular biomarkers in tears can provide reliable and accurate diagnosis and management of DED. This article introduces a porous microneedle-assisted electrochemical aptamer biosensor for the collection and quantitative analysis of DED-associated biomarkers in tears. The porous microneedle component collects tears while the electrochemical aptamer sensor detects interferon-gamma (IFN- $\gamma$ ), tumor necrosis factor-alpha (TNF- $\alpha$ ), and matrix metalloproteinase-9 (MMP-9) with the detection limit of 4.46 pg mL<sup>-1</sup>, 1.56 pg mL<sup>-1</sup>, and 4.97 ng mL<sup>-1</sup>, respectively. Clinically, DED is associated with 13 pg mL<sup>-1</sup> of IFN- $\gamma$ , 4 pg mL<sup>-1</sup> of TNF- $\alpha$ , and MMP-9 concentrations of more than 40 ng mL<sup>-1</sup> in tears, which are above the detection limits of our sensors. By taking MMP-9 as a model biomarker, we demonstrate a complete collection-to-detection workflow using this microneedle-aptamer biosensing device, which would facilitate the realization of point-of-care monitoring of DED.

In 2017, the Tear Film and Ocular Surface Society Dry Eye WorkShop II reached consensus upon the vicious circle of inflammation-driven tear film abnormalities.<sup>1</sup> Clinical results show that DED leads to ocular inflammation and subsequently elevated secretion of molecules like lactoferrin, matrix metalloproteinase-9 (MMP-9), interleukin-6 (IL-6), interferon-gamma (IFN- $\gamma$ ), and tumor necrosis factor-alpha (TNF- $\alpha$ ).<sup>4</sup> The levels of these biomolecules can indicate normal or pathogenic processes and the response to a therapeutic intervention. This provides a great opportunity for researchers to pursue the point-of-care (POC) of DED by quantifying these biomolecules (biomarkers) with portable devices. For example, Lu *et al.* developed a silicon nanowire immunosensor for the quantitative detection of MMP-9, demonstrating the feasibility of miniaturized antibody-based assays.<sup>5</sup> Wang *et al.* developed an aptamer-based biosensor that specifically recognized TNF- $\alpha$  with a detection limit of 0.34 pM in undiluted artificial tears.<sup>6</sup> The scientific exploration has led to the commercialization of devices like InflammDry®.

Despite these exciting advancements, most diagnostic methods still require professional medical staff and additional tear-sampling tools such as glass capillary tubes or Schirmer's strips. For example, in the InflammDry® test, a medical professional has to collect tears from the patient's eye by placing a fleece in the lower palpebral conjunctiva.<sup>7</sup> This often leads to sample loss, biomarker retention, and ocular irritation, while also complicating the overall workflow. It also limits the practicality of DED self-assessment.

To address this overlooked issue, we introduce a microneedle (MN)-based biosensor to achieve a collection-to-detection workflow (Fig. 1). The system is composed of a porous MN array for tear sampling and an aptamer-functionalized electrochemical sensor for downstream biomarker detection. The MN array, as reported in our previous work, is soft and light in weight, with anisotropic

## 1. Introduction

Dry eye disease (DED) is a common ocular disorder characterized by tear film instability and symptoms such as ocular discomfort, photophobia, and visual disturbance.<sup>1</sup> Owing to lifestyle changes associated with prolonged screen use, there is an increasing global prevalence of DED, with an estimated 10–20% in the population of over the age of 40, and 5.5–23.1% in children.<sup>2,3</sup> Current diagnosis of DED relies on laborious tests such as slit-lamp examination, fluorescein staining, and tear film breakup time. Even the most accessible method, the Schirmer's test, measures only the tear volume and correlates poorly with disease severity, limiting its value for DED grading or monitoring.

Department of Biomedical Engineering, College of Biomedicine, City University of Hong Kong, 83 Tat Chee Avenue, Kowloon Tong, Hong Kong SAR, P. R. China.  
 E-mail: yusong@cityu.edu.hk, chenjie.xu@cityu.edu.hk

<sup>†</sup> These authors contributed equally.





TNF- $\alpha$ -binding RNA aptamer: 5'GGAGUAUCUGAUGACAAUUCGGAGCUCC-SH-C6-3';

MMP-9-binding DNA aptamer: 5'-SH-C6-TCGTATGGCACGGGGTTGGTGTGGGTTGG-3'.

## 2.2. Electrochemical aptamer-based sensor fabrication

The fabrication began with 3D printing L-shaped polylactic acid (PLA) supports (7.5 mm length  $\times$  4 mm width and 7.5 mm length  $\times$  20 mm height, 1.75 mm thickness) with two 0.5 mm wide indentations that ran along the entire surface. After applying gold leaf adhesive and drying at room temperature overnight, masking tape (0.5 mm width) was applied along the indentations as outlined on the L-shaped structure. Gold leaf (Au) was then affixed onto the support. Silver/silver chloride (Ag/AgCl) paste was applied on the entire reference electrode (RE), while Ag paste was applied only on the long side of the working and counter electrodes (WE and CE). The masking tape was carefully removed before curing in 75 °C for around 20 min until it dried. Around 2/3 of the electrode areas on the longer side with Ag and Ag/AgCl paste was covered with epoxy glue for protection, leaving the ends exposed for electrochemical workstation connection. A three-electrode system was created after drying at room temperature for 12 h.

Before the addition of aptamers, Au electrodes were cleaned in a mild "piranha" solution with a 3:1 ratio of 50 mM sulphuric acid (H<sub>2</sub>SO<sub>4</sub>) and 25% w/v hydrogen peroxide (H<sub>2</sub>O<sub>2</sub>), followed by rinsing in deionized water and 75% ethanol.<sup>9</sup> The assembly of aptamers onto the Au WE was prepared according to the procedure outlined in the literature by Liu *et al.*<sup>10</sup> The aptamer solution was first heated to 95 °C for 10 min and gradually cooled to room temperature before use. Before immobilizing aptamers onto the WE, 0.02 M aptamer stock solution was reduced in 10 mM tris-(2-carboxyethyl) phosphine hydrochloride (TCEP) for 1 h. The thiolated aptamer solution was then diluted in 10 mM HEPES with 150 mM NaCl to the required concentrations of 1–5  $\mu$ M. The WE was incubated in the aptamer solution at 4 °C for 16 h. The electrodes were then rinsed with deionized water, and 3 mM 6-mercapto-1-hexanol (MCH) was added to the WE for 1 h. Finally, the electrodes were rinsed again and stored at 4 °C prior to use.

## 2.3. Morphological characterization of the sensor by SEM and EDS

The surface of the aptamer-modified WE before and after undergoing square wave voltammetry (SWV) measurement was imaged using a field-emission scanning electron microscope (SEM) (FEI Quanta 250). The unmodified Au WE surface was analyzed with energy dispersive X-ray spectroscopy (EDS) on the same equipment.

## 2.4. Surface-enhanced Raman spectroscopy

Surface-enhanced Raman spectroscopy was done using a WiTec Raman System at an excitation wavelength of 633 nm.

A large area scan was carried out on the surface of the aptamer modified WE (20  $\times$  20  $\mu$ m) with 20 points per line, 20 lines per image, and an integration time of 3 s. The resulting data and images were processed using WiTec Project 5.1.

## 2.5. Sensor characterization

All electrochemical measurements were done with a CHI 760E electrochemical analyzer workstation (CH Instruments). All measurements were carried out in 5 mM ferri/ferrocyanide (Fe(CN)<sub>6</sub><sup>3-/4-</sup>) buffer with 0.1 M potassium chloride (KCl) and 0.1 M potassium nitrate (KNO<sub>3</sub>). Cyclic voltammetry (CV) was carried out from -1 V to 1 V at a scan rate of 0.1 V s<sup>-1</sup> and 10<sup>-4</sup>. A sensitivity on the same sensor before and after cleaning with mild "piranha" solution, after the addition of aptamer and after incubation in MCH. Electrochemical impedance spectroscopy (EIS) was completed as well for the same electrode modification steps on one sensor under the parameters of 0.1 to 100 000 Hz and a 0.005 V amplitude. SWV at 60 Hz and 40 mV amplitude over -0.05 V to 0.35 V was done on bare electrodes, as well as after aptamer-MCH modification and after addition of the target biomarker on the same sensor.

## 2.6. Aptamer density optimization and sensor performance

We prepared sensors with different aptamer concentrations of 1, 3, and 5  $\mu$ M. The sensors were first placed in 10 mM HEPES buffer with 150 mM NaCl for 15 min to equilibrate. The initial voltammogram was obtained *via* SWV in 5 mM ferricyanide buffer, with an amplitude of 40 mV at 60 Hz over -0.05 V to 0.35 V *vs.* Ag/AgCl. The sensors were incubated with the target analytes under different concentrations in HEPES buffer for 15 min before performing SWV again with the same parameters. For human recombinant IFN- $\gamma$ , 1, 5, 10, 15, and 20 pg mL<sup>-1</sup> were used. For human recombinant TNF- $\alpha$ , 0.1, 0.5, 1, 5, and 10 pg mL<sup>-1</sup> were prepared. As for human recombinant MMP-9, concentrations of 10, 20, 30, 40, and 50 ng mL<sup>-1</sup> were tested. The same biomarker concentrations were used when measuring sensor performance. The resulting relative peak-current difference ( $\Delta i/i_0$ ) was calculated based on the relative peak currents before ( $i_0$ ) and after reacting with the target ( $i_{\text{target}}$ ) following the equation below.

$$\Delta i/i_0 = \frac{i_0 - i_{\text{target}}}{i_0}$$

## 2.7. Selectivity and anti-interference performance

We studied the SWV responses of IFN- $\gamma$  sensors before and after reacting with 50 ng mL<sup>-1</sup> IgE, 0.2 mM glucose, 10 pg mL<sup>-1</sup> TNF- $\alpha$ , 40 ng mL<sup>-1</sup> MMP-9, and 5 pg mL<sup>-1</sup> IFN- $\gamma$  in Fe(CN)<sub>6</sub><sup>3-/4-</sup>. Similarly, the TNF- $\alpha$  sensor responses before and after incubation in 50 ng mL<sup>-1</sup> IgE, 0.2 mM glucose, 20 pg mL<sup>-1</sup> IFN- $\gamma$ , 40 ng mL<sup>-1</sup> MMP-9, and 0.5 pg mL<sup>-1</sup> TNF- $\alpha$  were compared. For MMP-9 sensors, the experiment was completed with 50 ng mL<sup>-1</sup> IgE, 0.2 mM glucose, 20 pg mL<sup>-1</sup> IFN- $\gamma$ , 10 pg mL<sup>-1</sup> TNF- $\alpha$ , and 20 ng mL<sup>-1</sup> MMP-9. The anti-interference performance was



measured through SWV after allowing each sensor to react in a solution with interfering molecules. The solution was prepared in HEPES with  $50 \text{ ng mL}^{-1}$  IgE,  $0.2 \text{ mM}$  glucose,  $1 \text{ pg mL}^{-1}$  IFN- $\gamma$ ,  $0.1 \text{ pg mL}^{-1}$  TNF- $\alpha$ , and  $10 \text{ ng mL}^{-1}$  MMP-9. The results ( $\Delta i/i_0$ ) were then compared to that of the target marker only at the same concentration.

## 2.8. Repeatability

The SWV current without the target was first collected after the fabrication of aptamer sensors. Each sensor was allowed to incubate with the target biomarker ( $5 \text{ pg mL}^{-1}$  IFN- $\gamma$ ,  $0.5 \text{ pg mL}^{-1}$  TNF- $\alpha$ , or  $20 \text{ ng mL}^{-1}$  MMP-9) for 15 min before 3

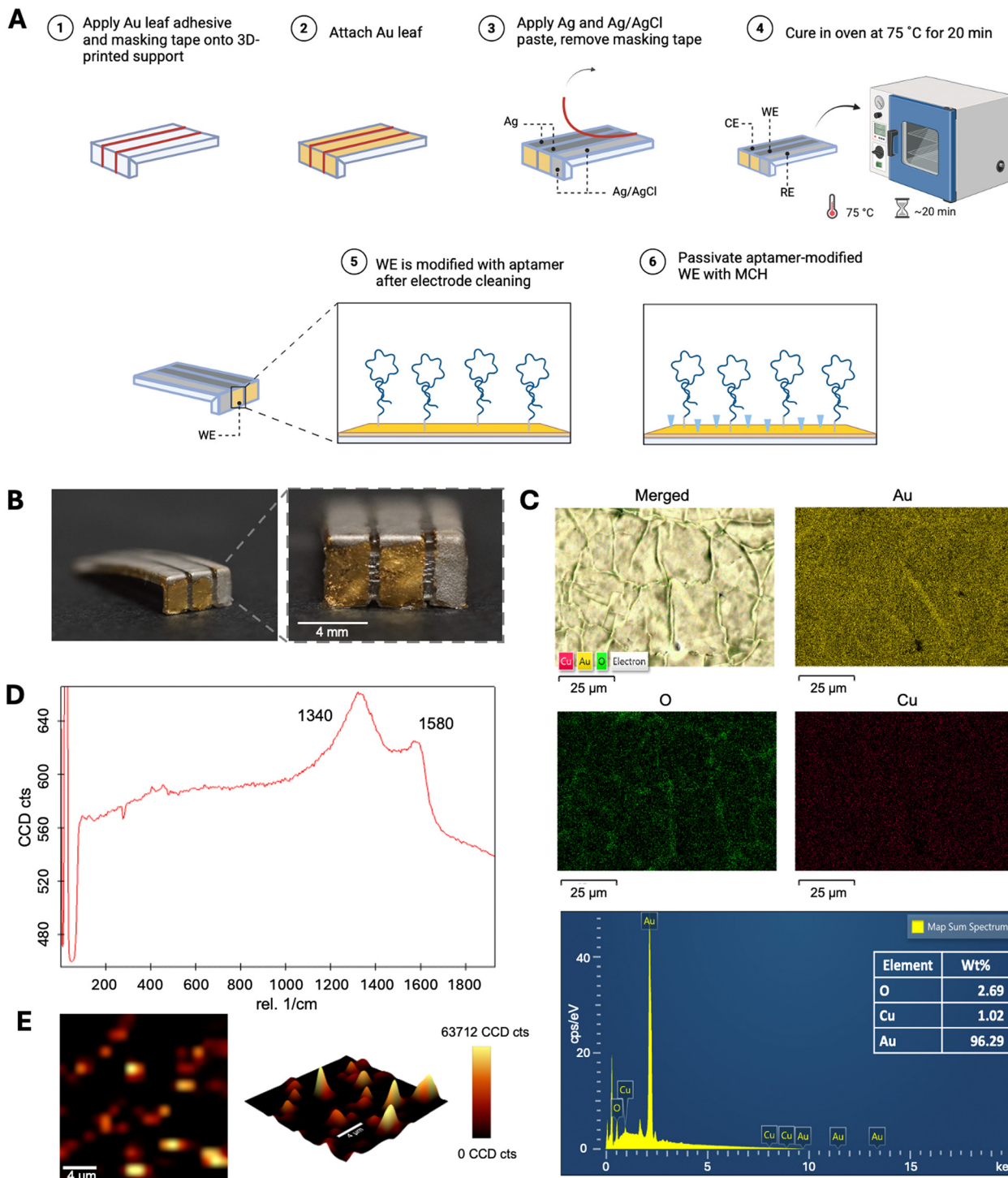


**Fig. 2** Development and surface characterization of the electrochemical aptamer sensor: (A) schematic illustration of the fabrication process; (B) images of the Au leaf electrodes, scale bar: 4 mm; (C) EDS of the bare Au WE; (D) Raman spectrum of the aptamer modified WE; (E) 2D and 3D Raman mapping based on the intensity of the  $1340 \text{ cm}^{-1}$  peak.



consecutive SWV measurements. The repeatability was presented as the relative peak current difference ( $\Delta i/i_0$ ) of the 3 consecutive measurements in each sensor.

### 2.9. Fabrication of MN patches

MN patches ( $1 \times 10$  array, with a tip length of  $1000 \mu\text{m}$ ) were fabricated following the procedure from our previous work.<sup>8</sup> In short,  $10 \mu\text{L}$  of a prepolymer solution containing 5% wt gelatin and 1 M EDC/NHS were added into each PDMS-negative MN mold before centrifuging at 4000 rpm for 3 min to fill the tips. After filling up the rest of the molds (the base) with an additional  $30 \mu\text{L}$  of the prepolymer solution, they were cooled unidirectionally originating from the base in a cooling bath at  $-20 \text{ }^\circ\text{C}$ . The molds were subsequently left at  $-20 \text{ }^\circ\text{C}$  for 48 h and submerged in deionized water at room

temperature for 16 h. After freeze-drying at  $-80 \text{ }^\circ\text{C}$  for 4 h and demolding, porous MN patches were obtained.

### 2.10. Morphological characterization of porous MN by SEM

The morphology of MN was imaged with a field-emission scanning electron microscope (SEM) (FEI Quanta 250). The needles were cut and removed from the base, while the MN base was cut perpendicularly to reveal the internal structures. All samples were sputter coated with a 10 nm gold layer for SEM imaging.

### 2.11. Integration of MN with aptamer sensors for DED biomarker collection and detection in the hydrogel model

After the preparation of aptamer sensors, SWV measurements of each sensor was first recorded in  $\text{Fe}(\text{CN})_6^{3-/4-}$  as the

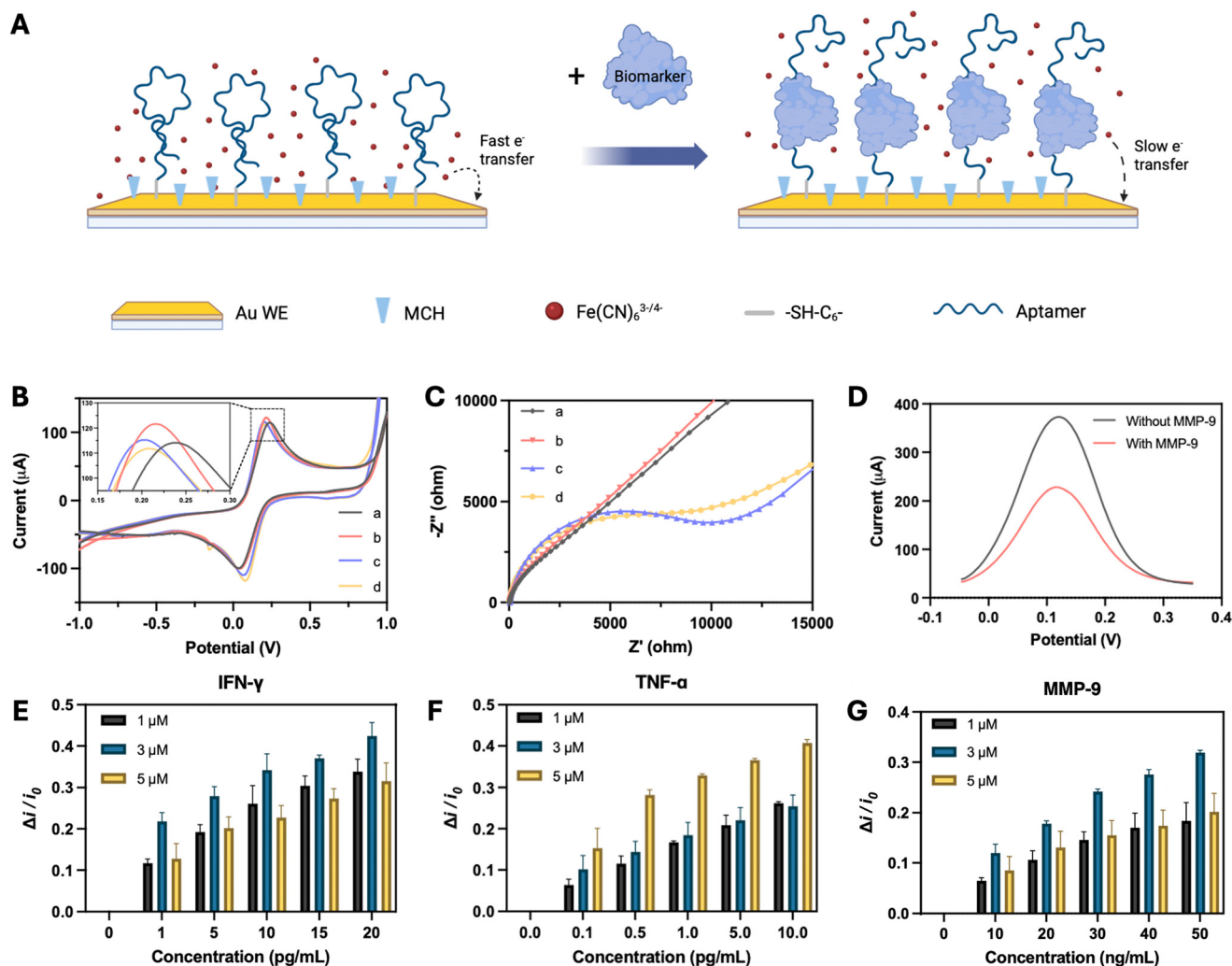


**Fig. 3** Electrochemical characterization and optimization of the electrochemical aptamer sensor: (A) working principle; (B) CV and (C) EIS of the electrode after each modification step, (a) bare Au WE, (b) Au WE after cleaning, (c) aptamer-functionalized WE, (d) aptamer/MCH-modified WE; (D) SWV responses of the MMP-9 aptamer sensor with and without  $50 \text{ ng mL}^{-1}$  MMP-9; (E) optimization of the IFN- $\gamma$  aptamer concentration (1, 3, and  $5 \mu\text{M}$ ), where the biomarker IFN- $\gamma$  concentration changes from 0 to  $20 \text{ pg mL}^{-1}$ ; (F) optimization of the TNF- $\alpha$  aptamer concentration (1, 3, and  $5 \mu\text{M}$ ), where the biomarker TNF- $\alpha$  concentration changes from 0 to  $10 \text{ pg mL}^{-1}$ ; (G) optimization of the MMP-9 aptamer concentration (1, 3, and  $5 \mu\text{M}$ ), where the biomarker MMP-9 concentration changes from 0 to  $50 \text{ ng mL}^{-1}$ .



baseline before integration with MN. To assemble the device, the MN patch was attached on top of the aptamer sensor using a 3M™ double-sided medical adhesive along the indentations in between the electrode areas (Fig. 5A). We then set up a model system using 0.4% agarose gel.<sup>11</sup> 10  $\mu\text{L}$  of artificial tears with various levels of recombinant human MMP-9 (10, 20, 30, 40,

and 50  $\text{ng mL}^{-1}$ ) were added onto the agarose gel model to simulate the healthy eye and dry eye (HE and DE). The artificial tears were then collected from the agarose gel model by placing the MN patch for approximately 3 min. The device was then left in  $\text{Fe}(\text{CN})_6^{3-/4-}$  buffer for 15 min before electrochemical measurements. The SWV results ( $\Delta i/i_0$ ) were calculated based on the baseline SWV

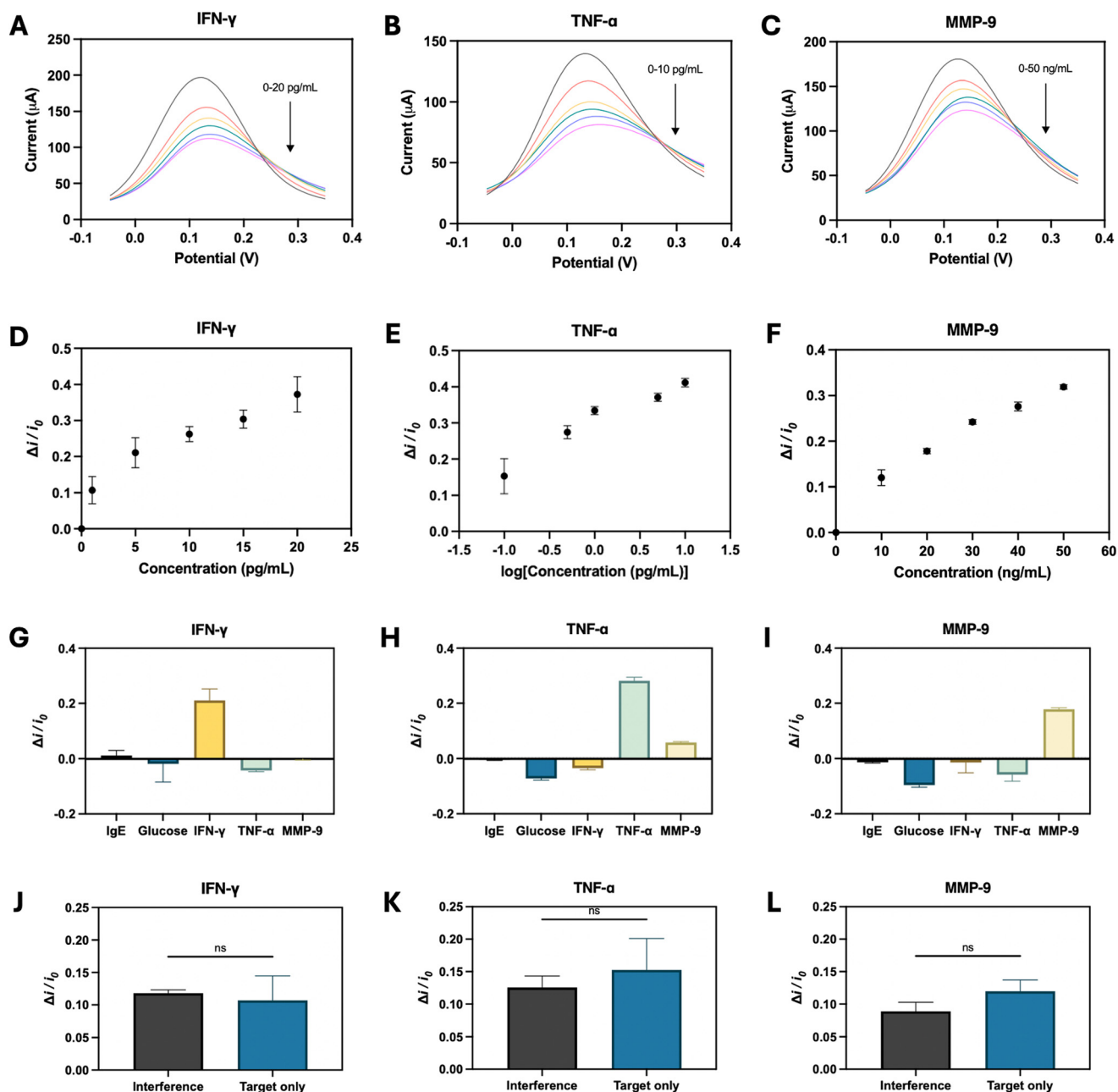
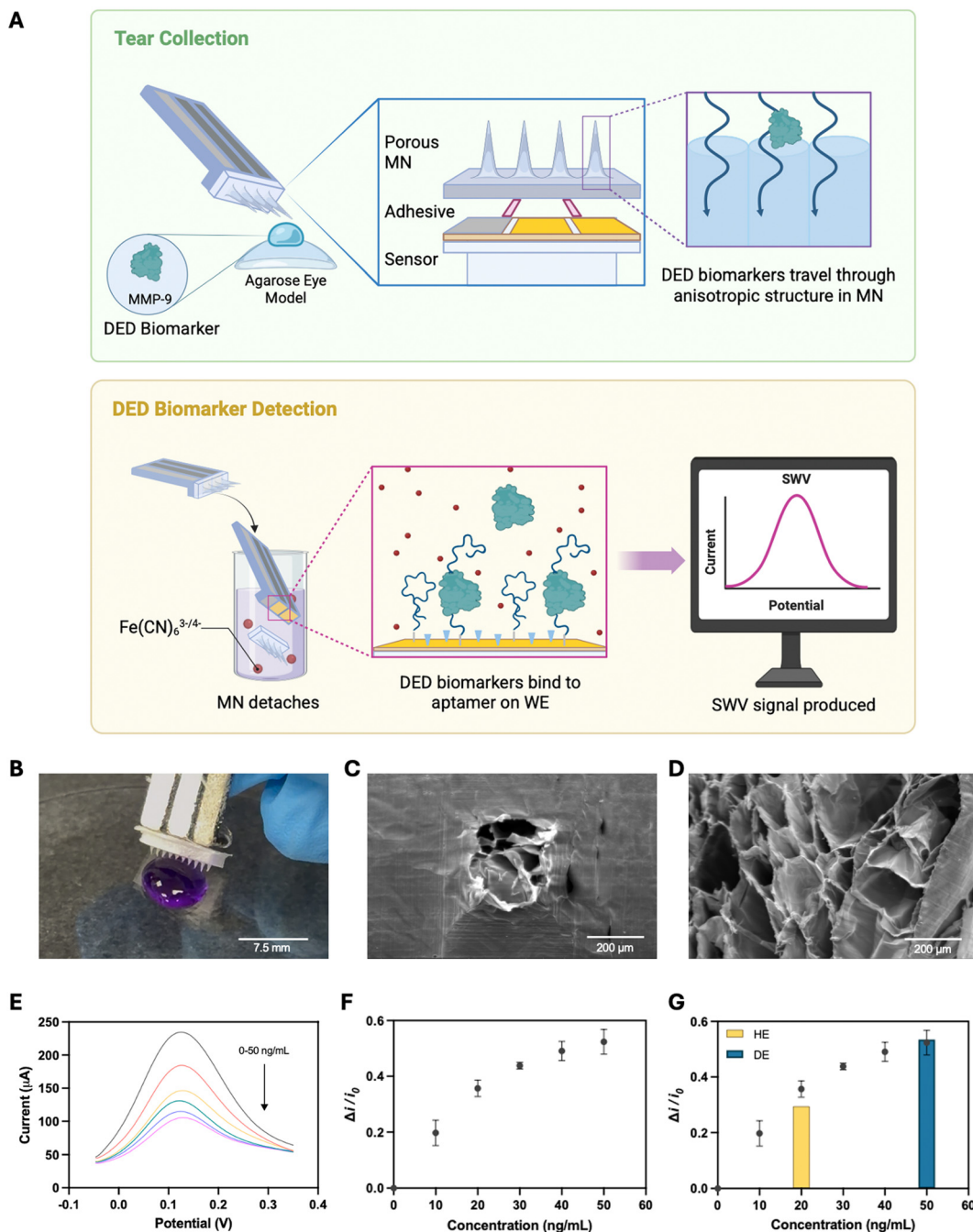


Fig. 4 Characterization of the sensor sensitivity and selectivity: SWV responses of (A) IFN- $\gamma$  sensor in 0–20  $\text{pg mL}^{-1}$  IFN- $\gamma$ , (B) TNF- $\alpha$  sensor in 0–10  $\text{pg mL}^{-1}$  TNF- $\alpha$ , and (C) MMP-9 sensor in 0–50  $\text{ng mL}^{-1}$  MMP-9; calibration curves of (D) IFN- $\gamma$  sensor, (E) TNF- $\alpha$  sensor, and (F) MMP-9 sensor; (G) specificity of IFN- $\gamma$  sensor to 50  $\text{ng mL}^{-1}$  IgE, 0.2 mM glucose, 5  $\text{pg mL}^{-1}$  IFN- $\gamma$ , 10  $\text{pg mL}^{-1}$  TNF- $\alpha$ , and 40  $\text{ng mL}^{-1}$  MMP-9; (H) specificity of TNF- $\alpha$  sensor to 50  $\text{ng mL}^{-1}$  IgE, 0.2 mM glucose, 20  $\text{pg mL}^{-1}$  IFN- $\gamma$ , 0.5  $\text{pg mL}^{-1}$  TNF- $\alpha$ , and 40  $\text{ng mL}^{-1}$  MMP-9; (I) specificity of MMP-9 sensor to 50  $\text{ng mL}^{-1}$  IgE, 0.2 mM glucose, 20  $\text{pg mL}^{-1}$  IFN- $\gamma$ , 10  $\text{pg mL}^{-1}$  TNF- $\alpha$ , and 20  $\text{ng mL}^{-1}$  MMP-9; anti-interference performance in interfering solution (50  $\text{ng mL}^{-1}$  IgE, 0.2 mM glucose, 1  $\text{pg mL}^{-1}$  IFN- $\gamma$ , 0.1  $\text{pg mL}^{-1}$  TNF- $\alpha$ , and 10  $\text{ng mL}^{-1}$  MMP-9) of (J) IFN- $\gamma$  sensor against 1  $\text{pg mL}^{-1}$  IFN- $\gamma$ , (K) TNF- $\alpha$  sensor against 0.1  $\text{pg mL}^{-1}$  TNF- $\alpha$ , and (L) MMP-9 sensor against 10  $\text{ng mL}^{-1}$  MMP-9.





**Fig. 5** MN-integrated MMP-9 sensor device performance *in vitro*. (A) Schematic illustration of the workflow of the integrated device; (B) digital image of the MN collecting liquid dye, scale bar: 7.5 mm; (C) SEM image of the internal microstructure of MN; (D) SEM image of the cross section of MN, scale bar: 200  $\mu\text{m}$ ; (E) SWV of the integrated MMP-9 sensor device; (F) calibration curve of the MMP-9 sensor device using artificial tears; (G) measurements of simulated HE and DE artificial tear samples compared to the calibration curve.

measurements recorded previously to obtain a standard curve.

Two individual samples of 20  $\text{ng mL}^{-1}$  and 50  $\text{ng mL}^{-1}$  of MMP-9 in artificial tears were prepared to represent HE tears and DE tears respectively. Using the integrated device, the artificial samples were recovered from the hydrogel model for SWV measurements in the same manner.

## 2.12. Statistical analysis

Each experiment was repeated at least 3 times. All data were shown as the mean  $\pm$  SD unless specified otherwise. Quantitative analysis was based on Welch's *t*-test to determine the *p* values. In all cases,  $p < 0.05$  was considered statistically significant (\* $p < 0.05$ , \*\* $p < 0.01$ , \*\*\* $p < 0.001$ , ns: not significant).



### 3. Results and discussion

#### 3.1. Development of the electrochemical aptamer sensor

We developed an L-shaped electrochemical aptamer sensor as the biomarker detection module (Fig. 2A). The L-shaped geometry provides mechanical support and enables the integration with the MN array during tear sampling. This L-shaped structure was 3D-printed using PLA, with indentations incorporated to spatially separate the electrodes, prevent electrical shorting, and reduce signal interference. The electrochemical electrodes were fabricated using Au leaf, Ag/AgCl paste, and Ag paste. Au leaf was first laminated onto the PLA substrate to define the regions of the WE, CE, and RE. Ag/AgCl paste was subsequently applied to the designated RE region to construct the Ag/AgCl reference electrode, while the Au-leaf-based WE and CE surfaces were retained as the active sensing interfaces. To stabilize conductivity and minimize side reactions during electrochemical measurements, the non-sensing areas of the WE and CE were coated with Ag paste and sealed with epoxy. This ultimately provided a three-electrode system consisting of the WE and CE against the Ag/AgCl RE (Fig. 2B). The use of 23 kt Au leaf, which has a purity of 95.8%, in the fabrication of the electrochemical sensor has been shown to exhibit similar electrochemical behaviour as commercial screen-printed electrodes.<sup>12</sup> The composition of the Au-leaf-based WE was verified through EDS. The electrode surface is mainly composed of Au (96.69 wt%), with only small traces of copper (Cu) and oxygen (O) that are generally present in commercial Au screen-printed electrodes<sup>9,12</sup> (Fig. 2C).

The next step is to functionalize the Au WE with the aptamer. The aptamer has been reported as the effective bioreceptor for inflammatory biomarkers, and its binding-induced conformational change can be transduced into electrochemical signals.<sup>10</sup> In the tears of patients with DED, the IFN- $\gamma$  level increases from  $\sim 4$  pg mL<sup>-1</sup> to  $\sim 13$  pg mL<sup>-1</sup>, the TNF- $\alpha$  level increases from  $<0.5$  pg mL<sup>-1</sup> to  $\sim 4$  pg mL<sup>-1</sup>, and the MMP-9 level exceeds 40 ng mL<sup>-1</sup>.<sup>4,13,14</sup> Therefore, we synthesized thiolated aptamers with specificity to three biomarkers and immobilized them onto the Au WE *via* a standard thiol-based self-assembled monolayer formation process.<sup>5,10,15</sup> Briefly, aptamers with thiol modifications were first reduced in TCEP solution to cleave disulfide bonds, ensuring exposure of free thiol groups for Au binding. The aptamer solution was then diluted to the desired concentration of 1–5  $\mu$ M in HEPES buffer and was casted on the surface of the WE for 16 h. After immobilization, MCH was added to the WE to passivate unoccupied Au sites and promote the formation of a well-packed sensing layer.

The modified electrode surface was characterized using Raman imaging (Fig. 2D). Under 633 nm excitation, there were major peaks at 1340 and 1580 cm<sup>-1</sup>, which are associated with the C–N and C=N stretching modes found in both adenine and guanine.<sup>16</sup> This confirms the presence of aptamers on the WE surface. Based on the quantitative signal at 1340 cm<sup>-1</sup>, we could map the distribution of aptamers

across the WE surface in both 2D and 3D (Fig. 2E). In this case, 3  $\mu$ M of MMP-9 aptamer on the Au WE was mapped. It is expected that the distribution of aptamers will appear denser with a higher aptamer density such as 5  $\mu$ M, and more sparsely distributed on the surface with a lower aptamer density (*e.g.* 1  $\mu$ M).

#### 3.2. Electrochemical characterization of the functionalized electrode interface

We investigated how the formation of the aptamer/MCH monolayer modulated electron transfer at the electrode interface using the MMP-9 aptamer as an example. To confirm the stepwise surface modification on the WE, CV and EIS were performed in the buffer with 5 mM Fe(CN)<sub>6</sub><sup>3-/4-</sup>, 0.1 M KCl and 0.1 M KNO<sub>3</sub>, where the Fe(CN)<sub>6</sub><sup>3-/4-</sup> redox couple underwent reversible electron transfer interacting with the electrode surface (Fig. 3A). In CV, the bare Au electrode exhibited high anodic peak currents at approximately 0.2 V due to rapid electron transfer. After electrode cleaning, the peak current increased compared to that of the bare Au electrode as the surface resistance was reduced. Aptamer immobilization subsequently lowered the peak current, and additional current suppression was observed after MCH backfilling, which is consistent with the increased interfacial resistance caused by the formation of a compact SAM (Fig. 3B). Correspondingly, in the Nyquist plots, the straight lines at an angle for the bare Au WE and after cleaning reflected the low charge transfer resistance of the system. The slope became slightly steeper as the surface resistance was lowered after electrode cleaning. Following aptamer immobilization, the graph displayed a semicircle trend, indicating a shift in surface chemistry and higher charge transfer resistance on the WE. The resistance was further increased with the formation of the MCH monolayer as observed by the larger semicircle diameter (Fig. 3C).

After validating the surface modification, SWV was used to verify the functionality of the aptamer-based sensing interface for DED biomarker detection. SWV responses with a frequency of 60 Hz and an amplitude of 40 mV were recorded for the MMP-9 aptamer sensor after incubation with and without the target, 50 ng mL<sup>-1</sup> of MMP-9 (Fig. 3D). The voltage range was defined as  $-0.05$  V to 0.35 V according to the anodic peak position in the CV results (Fig. 3B). A decrease in the SWV peak position from around 373  $\mu$ A to 227  $\mu$ A appeared after target binding, reflecting the slowed down electron-transfer process of the Fe(CN)<sub>6</sub><sup>3-/4-</sup> redox probe. When aptamers bind to their target analyte, the conformational change of aptamers would hinder the redox probes from interacting with the electrode surface, leading to a reduction in the faradic current. These results collectively confirm that the ability of the Au-leaf aptamer sensor in providing a stable functionalized interface and reliable electrochemical response for DED biomarker detection.

In addition, we examined the morphology of the WE surface before and after electrochemical interrogation with



the target analyte, MMP-9, using SEM (Fig. S1). Though some folds and cracks existed on the WE surface from the Au leaf application during fabrication, no significant structural damage occurred during sensing process. Despite imperfections, the Au-leaf electrodes exhibited sufficient structural integrity and robustness for the use of a disposable and low-cost sensor.

### 3.3. Optimization of the aptamer density on the sensing interface

We further optimized the aptamer concentration on the WE. Low aptamer coverage leads to insufficient target capture, whereas an overly dense aptamer layer impedes electron transfer and reduces the dynamic signal window. The ideal aptamer density should produce the largest current decrease upon target binding. We functionalized WEs with 1, 3, or 5  $\mu\text{M}$  of IFN- $\gamma$ , TNF- $\alpha$ , and MMP-9 aptamers, and then measured their SWV responses in 5 mM  $\text{Fe}(\text{CN})_6^{3-/4-}$  buffer before and after incubation with biomarker solutions spanning healthy and dry-eye tear levels (1–20  $\text{pg mL}^{-1}$  IFN- $\gamma$ , 0.1–10  $\text{pg mL}^{-1}$  TNF- $\alpha$ , and 10–50  $\text{ng mL}^{-1}$  MMP-9) (Fig. S2). To quantitatively compare aptamer loadings, signal suppression was analyzed through the relative peak-current change ( $\Delta i/i_0$ ), where  $i_0$  is the initial current measured before target binding, and  $\Delta i$  is the difference in peak current before and after incubation with each biomarker solution (Fig. 3E–G). Across all densities tested for each aptamer sensor, the difference in relative peak current increased progressively with increasing biomarker concentration, reflecting the enhanced electron-transfer blockage caused by aptamer–target binding. Among the concentrations tested, the overall trend showed that 3  $\mu\text{M}$  of IFN- $\gamma$  aptamer, 5  $\mu\text{M}$  of TNF- $\alpha$  aptamer, and 3  $\mu\text{M}$  of MMP-9 aptamer had the largest current suppression across their respective analyte ranges. Therefore, these aptamer concentrations provided the highest sensitivity and were applied in the subsequent experiments. Together, these results demonstrate that the optimization of the aptamer surface density is critical for maximizing signal responsiveness and establishing a robust electrochemical sensing interface for DED tear biomarkers.

### 3.4. Analytical performance of the aptamer sensors

Based on the SWV responses of the optimal sensors (*i.e.* 3  $\mu\text{M}$  of IFN- $\gamma$  aptamer, 5  $\mu\text{M}$  of TNF- $\alpha$  aptamer, and 3  $\mu\text{M}$  of MMP-9 aptamer) when exposed to different target concentrations in 5 mM  $\text{Fe}(\text{CN})_6^{3-/4-}$  buffer (Fig. 4A–C), the relationship between biomarker concentration ( $C$ ) and relative peak-current differences ( $\Delta i/i_0$ ) were reconstructed into calibration curves for analysis. The IFN- $\gamma$  aptamer sensor exhibited a linear relationship where the calibration curve was fitted to a line with the equation:  $\Delta i/i_0 = 0.01291 \times C_{\text{IFN-}\gamma} + 0.1196$ , and an  $R^2$  of 0.86 (Fig. 4D). Similarly, the TNF- $\alpha$  sensor calibration curve displayed a linear regression with the equation:  $\Delta i/i_0 = 0.12 \times [\log(C_{\text{TNF-}\alpha})] + 0.3008$ , and an  $R^2$  of 0.90 (Fig. 4E). The MMP-9 sensor was calibrated to a line

of  $\Delta i/i_0 = 0.004966 \times C_{\text{MMP-9}} + 0.07803$ , and an  $R^2$  of 0.97 (Fig. 4F). The limit of detection (LOD) for each sensor was calculated based on the standard deviation and the slope of the calibration curve. The LOD of the IFN- $\gamma$ , TNF- $\alpha$ , and MMP-9 sensors was 4.46  $\text{pg mL}^{-1}$ , 1.56  $\text{pg mL}^{-1}$ , and 4.97  $\text{ng mL}^{-1}$ , respectively. It should be noted that the LOD of TNF- $\alpha$  is higher than the healthy levels of less than 0.5  $\text{pg mL}^{-1}$ , causing limitations in the detection of subtle changes in healthy tears at low concentrations under the LOD. However, this LOD is sufficient for the monitoring of DED since it falls far below 4  $\text{pg mL}^{-1}$ , which is the level that is indicative of DED. Because DED is an inflammatory disease, the TNF- $\alpha$  tear levels is expected to increase even further as the disease progresses. These results reflect that all three aptamer sensors provide a sufficiently low LOD and broad dynamic ranges suitable for tear-based DED biomarker analysis.

To demonstrate the specificity, each sensor was challenged with individual non-specific tear components at concentrations representative of physiological tear backgrounds, including 50  $\text{ng mL}^{-1}$  IgE, 0.2 mM glucose, 20  $\text{pg mL}^{-1}$  IFN- $\gamma$ , 10  $\text{pg mL}^{-1}$  TNF- $\alpha$ , and 40  $\text{ng mL}^{-1}$  MMP-9. The responses were then compared to the respective analyte of interest at a lower concentration, *i.e.* 5  $\text{pg mL}^{-1}$  IFN- $\gamma$ , 0.5  $\text{pg mL}^{-1}$  TNF- $\alpha$ , or 20  $\text{ng mL}^{-1}$  MMP-9. As shown in Fig. 4G–I, all sensors displayed a specific response to the corresponding analytes as reflected by the greatest decrease in the current compared to the other non-specific analytes, demonstrating their strong specificity. However, it was observed that in the presence of non-specific molecules, especially glucose, the sensors showed a negative response (*i.e.* an increase in current). This is potentially caused by the electrostatic interaction between the molecules and aptamers. In the case of glucose, it has been reported that the small molecule could interfere and increase electron transfer, leading to an increase in the current. Meanwhile, other biomolecules could cause biofouling or reduced electrical repulsion due to their nature, generating a negative response.<sup>17,18</sup> Therefore, to further evaluate the sensing performance in more complex environments, the anti-interference performance of the sensors was investigated by incubating each target biomarker together with a mixture of all the non-specific tear components. The signal response was compared to that of only the target at the same concentration in HEPES buffer (Fig. 4J–L). There was no significant difference between the two groups for all sensors, indicating that coexisting tear constituents do not impede target recognition or electron-transfer processes. While the effect of non-specific markers is limited in the current sensors, the application of nanostructure strategies could be explored to further improve the aptamer sensor performance and minimize non-specific responses.<sup>19</sup>

### 3.5. Reproducibility of the aptamer sensors

The reproducibility of the Au leaf aptamer sensors was assessed (Fig. S3). 3 of each aptamer sensor (IFN- $\gamma$ , TNF- $\alpha$ , and MMP-9) were fabricated at the same time. After



incubation with the same target analyte concentration (5 pg mL<sup>-1</sup> IFN- $\gamma$ , 0.5 pg mL<sup>-1</sup> TNF- $\alpha$ , or 20 ng mL<sup>-1</sup> MMP-9), 3 consecutive SWV measurements in Fe(CN)<sub>6</sub><sup>3-/4-</sup> buffer were completed for each individual sensor, obtaining 3 relative peak-current difference values. The means of the repeated responses were compared. Even at lower biomarker concentrations, each group was able to produce similar electrochemical responses. The results demonstrated the reproducibility of the IFN- $\gamma$ , TNF- $\alpha$ , and MMP-9 aptamer sensors.

### 3.6. The integration of the MN and MMP-9 aptamer sensor

As a proof of concept, an MN array was integrated with the MMP-9 aptamer sensor to evaluate the practical performance of the device (Fig. 5A). In this configuration, the disposable integrated device consists of a porous MN array for tear collection, and an L-shaped sensor for biomarker detection (Fig. S4). The MN array (1 × 10), prepared as described in our previous work, is porous, soft, and compatible with the ocular surface. Its aligned microchannels enable rapid tear extraction through capillary action while showing high biomarker recovery efficiency (Fig. 5B–D).<sup>8</sup> After recording the baseline measurement, the MN patch is temporarily affixed to the sensor surface using a double-sided medical adhesive deposited within the predefined indentations (Fig. S5A and B). During use, tear fluid is first collected from the ocular surface with the MN on the integrated device (Video S1 and Fig. 5B and S5C). As the liquid travels from the tips to the base of the MN, tear biomarkers come into contact and interact with the aptamer-functionalized sensing interface (Fig. S5D). The device is then immersed in Fe(CN)<sub>6</sub><sup>3-/4-</sup> buffer, where the medical tape loses adhesion and the MN array detaches (Fig. S5E). Finally, electrochemical quantification is carried out (Fig. S5F). This detachable design allows tear collection and sensing to be carried out in a single workflow while ensuring minimal sample loss, providing a user-friendly disposable biosensor.

An ocular surface agarose gel model was used for the *in vitro* assessment of the integrated device (Fig. 5A).<sup>11</sup> Commercial artificial tears spiked with 10–50 pg mL<sup>-1</sup> human recombinant MMP-9, mimicking the tear states of the healthy eye and dry eye (HE and DE), were loaded onto an agarose gel eye model. The baseline SWV response of the MMP-9 aptamer sensor has been pre-recorded in Fe(CN)<sub>6</sub><sup>3-/4-</sup> buffer before integration of the MN patch onto the MMP-9 aptamer sensor. The MN array on the integrated device was placed on the agarose gel for 3 min, during which artificial tears was extracted through capillary-driven absorption. After collection, the device was immersed in Fe(CN)<sub>6</sub><sup>3-/4-</sup> buffer to enable MN detachment, and was left for 15 min to allow for sufficient incubation time on the sensing interface (Video S2). Then, SWV measurements were performed. The obtained responses were converted to quantitative concentrations and were fitted to a standard curve with the equation:  $\Delta i/i_0 = 0.007869 \times C_{\text{MMP-9}} + 0.1653$ , and an  $R^2$  of 0.86 (Fig. 5E and F).

Although the response was dampened when tested in artificial tears, presumably from the viscosity agents and other ingredients that could hinder electron transfer, the trend of the calibration curve mostly matched the standard results obtained previously.<sup>20</sup> Two additional artificial tear samples with 20 ng mL<sup>-1</sup> and 50 ng mL<sup>-1</sup> MMP-9 were prepared to represent tears from the HE and DE, respectively (Fig. 5G). The same collection-to-detection workflow was applied to measure the SWV responses of the samples. Based on the relative peak-current difference, the theoretical concentrations were calculated using the previously calibrated equation. For the HE sample, the measured  $\Delta i/i_0$  was 0.295, leading to a theoretical concentration of 16.5 ng mL<sup>-1</sup>. In the DE sample, a theoretical concentration of 46.9 ng mL<sup>-1</sup> was calculated from the measured  $\Delta i/i_0$ , 0.535. Compared to the actual concentrations of 20 ng mL<sup>-1</sup> and 50 ng mL<sup>-1</sup>, the accuracy is around 85–90%. While the accuracy of the MN-integrated sensor could be further improved, the results demonstrated the practicality of detecting HE and DE tears.

These *in vitro* experiments illustrated that even in a physiologically relevant model, the integrated porous MN and aptamer sensor platform can successfully collect and quantify MMP-9 in tears, supporting its potential for DED tear biomarker detection.

## 4. Conclusion

This work developed an MN-integrated electrochemical-based aptamer sensor for the detection of three dry eye disease biomarkers, IFN- $\gamma$ , TNF- $\alpha$ , and MMP-9. In this disposable device, a soft, porous MN patch with aligned microchannels functions as the tear extraction tool for the collection of tears from the ocular surface to the sensing interface. The sensing module consists of a three-electrode system made with Au leaf and thiolated aptamers that were attached through self-assembly. Fe(CN)<sub>6</sub><sup>3-/4-</sup> were utilized as redox probes to reflect the decrease in the faradic current using SWV as the aptamers bind to their target analytes. All three sensors were able to achieve a low LOD, specifically 4.46 pg mL<sup>-1</sup>, 1.56 pg mL<sup>-1</sup>, and 4.97 ng mL<sup>-1</sup> for IFN- $\gamma$ , TNF- $\alpha$ , and MMP-9 respectively, in addition to a linear range that covers the clinical concentrations (13 pg mL<sup>-1</sup> of IFN- $\gamma$ , 4 pg mL<sup>-1</sup> of TNF- $\alpha$ , and > 40 ng mL<sup>-1</sup> of MMP-9) for DED diagnosis. The aptamer sensors also demonstrated high selectivity, as well as good anti-interference performance in the presence of common tear components. As a proof of concept, the MMP-9 aptamer sensor was integrated with a porous MN patch for the collection and detection of MMP-9 in artificial tears, illustrating the complete workflow of this integrated system *in vitro*. While there are limitations in accuracy and quantification of tear volume, this disposable MN integrated device provides a promising direction for the point-of-care quantitative monitoring of DED.



## Conflicts of interest

The authors declare no conflict of interest.

## Data availability

Data for this article, including electrochemical data and original EDS and Raman spectroscopy data are available at Science Data Bank at <https://doi.org/10.57760/sciencedb.30014>. Supplementary information (SI) is available. See DOI: <https://doi.org/10.1039/d6lc00230g>.

## Acknowledgements

C. X. appreciates the support from the Research Impact Fund (R4020-22) and the General Research Fund (GRF) from the Research Grants Council (RGC) of the Hong Kong Special Administrative Region, China (CityU11202021, CityU11202222, CityU11100323, CityU11101324), and the National Science Fund for Distinguished Young Scholars from the National Natural Science Foundation of China (T2425004).

## References

- J. P. Craig, K. K. Nichols, E. K. Akpek, B. Caffery, H. S. Dua, C.-K. Joo, Z. Liu, J. D. Nelson, J. J. Nichols, K. Tsubota and F. Stapleton, TFOS DEWS II Definition and Classification Report, *Ocul. Surf.*, 2017, **15**, 276–283.
- A. C. Britten-Jones, M. T. M. Wang, I. Samuels, C. Jennings, F. Stapleton and J. P. Craig, Epidemiology and Risk Factors of Dry Eye Disease: Considerations for Clinical Management, *Medicina*, 2024, **60**, 1458.
- F. Stapleton, F. G. Velez, C. Lau and J. S. Wolffsohn, Dry eye disease in the young: A narrative review, *Ocul. Surf.*, 2024, **31**, 11–20.
- N. R. Kumar, M. Praveen, R. Narasimhan, P. Khamar, S. D'Souza, A. Sinha-Roy, S. Sethu, R. Shetty and A. Ghosh, Tear biomarkers in dry eye disease: Progress in the last decade, *Indian J. Ophthalmol.*, 2023, **71**, 1190–1202.
- Z. Lu, T. Liu, X. Zhou, Y. Yang, Y. Liu, H. Zhou, S. Wei, Z. Zhai, Y. Wu, F. Sun, Z. Wang, T. Li and J. Hong, Rapid and quantitative detection of tear MMP-9 for dry eye patients using a novel silicon nanowire-based biosensor, *Biosens. Bioelectron.*, 2022, **214**, 114498.
- Z. Wang, W. Dai, S. Yu, Z. Hao, R. Pei, C. G. De Moraes, L. H. Suh, X. Zhao and Q. Lin, Towards detection of biomarkers in the eye using an aptamer-based graphene affinity nanobiosensor, *Talanta*, 2022, **250**, 123697.
- G. Mejía-Salgado, W. Rojas-Carabali, C. Cifuentes-González, L. Zárate-Pinzón, C. A. Rodríguez-Rodríguez, G. Marroquín-Gómez, M. L. Moreno-Pardo, J. Tirado-Ángel and A. de-la-Torre, Real-world performance of the inflammadry test in dry eye diagnosis: an analysis of 1,515 patients, *Graefes Arch. Clin. Exp. Ophthalmol.*, 2025, **263**, 1623–1631.
- T. Hu, K. S. Lui, E. B. Ko, Y. Zhao, Q. Zhang, H. Yang, M. Zheng, H. Chang, B. Guo, A. K. L. Cheung and C. Xu, Microneedles with an anisotropic porous microstructure facilitate the transdermal delivery of small molecules, lipid nanoparticles, and T cells, *Matter*, 2025, **8**, 102038.
- L. M. Fischer, M. Tenje, A. R. Heiskanen, N. Masuda, J. Castillo, A. Bentien, J. Émneus, M. H. Jakobsen and A. Boisen, Gold cleaning methods for electrochemical detection applications, *Microelectron. Eng.*, 2009, **86**, 1282–1285.
- Y. Liu, N. Tuleouva, E. Ramanculov and A. Revzin, Aptamer-Based Electrochemical Biosensor for Interferon Gamma Detection, *Anal. Chem.*, 2010, **82**, 8131–8136.
- M. Cui, M. Zheng, C. Wiraia, S. W. T. Chew, A. Mishra, V. Mayandi, R. Lakshminarayanan and C. Xu, Ocular Delivery of Predatory Bacteria with Cryomicroneedles Against Eye Infection, *Adv. Sci.*, 2021, **8**, 2102327.
- M. S. F. Santos, W. A. Ameku, I. G. R. Gutz and T. R. L. C. Paixão, Gold leaf: From gilding to the fabrication of disposable, wearable and low-cost electrodes, *Talanta*, 2018, **179**, 507–511.
- D. C. Jackson, W. Zeng, C. Y. Wong, E. J. Mifsud, N. A. Williamson, C.-S. Ang, A. J. Vingrys and L. E. Downie, Tear Interferon-Gamma as a Biomarker for Evaporative Dry Eye Disease, *Invest. Ophthalmol. Vis. Sci.*, 2016, **57**, 4824.
- K.-C. Yoon, I.-Y. Jeong, Y.-G. Park and S.-Y. Yang, Interleukin-6 and Tumor Necrosis Factor- $\alpha$  Levels in Tears of Patients With Dry Eye Syndrome, *Cornea*, 2007, **26**, 431–437.
- Y. Liu, Q. Zhou and A. Revzin, An aptasensor for electrochemical detection of tumor necrosis factor in human blood, *Analyst*, 2013, **138**, 4321.
- W. Safar, A. Azziz, M. Edely and M. Lamy De La Chapelle, Conventional Raman, SERS and TERS Studies of DNA Compounds, *Chem*, 2023, **11**, 399.
- L.-D. Li, X.-J. Mu, M. Xie, Y. Peng, Z.-B. Chen, L. Guo and L. Jiang, Signal-On Architecture for Electrochemical Aptasensors Based on Multiple Ion Channels, *Anal. Chem.*, 2012, **84**, 10554–10559.
- Z. Chen, H. Li, M. Xie, F. Zhao and S. Han, Label-Free Electrochemical Aptasensor for Sensitive Detection of Malachite Green Based on AuNPs/MWCNTs@TiO<sub>2</sub> Nanocomposites, *Int. J. Mol. Sci.*, 2023, **24**, 10594.
- A. J. Ritz, O. M. Stuehr, D. N. Comer and R. A. Lazenby, Controlling Gold Morphology Using Electrodeposition for the Preparation of Electrochemical Aptamer-Based Sensors, *ACS Appl. Bio Mater.*, 2024, **7**, 1925–1935.
- P. Galek, A. Slesinski, K. Fic and J. Menzel, Peculiar role of the electrolyte viscosity in the electrochemical capacitor performance, *J. Mater. Chem. A*, 2021, **9**, 8644–8654.

